Nuclear Inst. and Methods in Physics Research, A 922 (2019) 28–35

Contents lists available at ScienceDirect

Nuclear Inst. and Methods in Physics Research, A

journal homepage: www.elsevier.com/locate/nima

Pepperpot emittance measurements of ion beams from an electron beam ion source

J. Pitters [a], M. Breitenfeldt [a], S. Duarte Pinto [b], H. Pahl [a,c], A. Pikin [a,d], A. Shornikov [a,e], F. Wenander [a,*]

[a] CERN, CH-1211 Geneva 23, Switzerland
[b] PHOTONIS, Dwazziewegen 2, 9301 ZR, Roden, Netherlands
[c] Heidelberg Graduate School of Fundamental Physics, Heidelberg University, Im Neuenheimer Feld 226, 69120 Heidelberg, Germany
[d] School of Physics and Astronomy, The University of Manchester, Manchester, M13 9PL, United Kingdom
[e] High Voltage Engineering Europa B.V., Amsterdamseweg 63, 3812 RR, Amersfoort, Netherlands

ARTICLE INFO

Keywords:
Pepperpot emittance meter
EBIS
Transverse emittance
Highly charged ions
MCP

ABSTRACT

A pepperpot emittance meter was used to measure the transverse emittance of multiply charged beams from REXEBIS, an Electron Beam Ion Source (EBIS) used for charge breeding of radioactive ion beams. The emittance meter is equipped with a Micro Channel Plate (MCP), a phosphor screen and a CCD camera for detection of the ion signal. The pulsed beam structure of low duty cycle imposes challenging constraints on the detector settings. In this article we give a careful analysis of the optimal operating parameters of the pepperpot emittance meter for ion beams of varying intensities. Emittance values for mass-separated and non-separated beams for different operating modes of the EBIS are presented. Furthermore we report on aberrations created in our injection/extraction system.

1. Introduction

REXEBIS [1] is used to perform charge breeding of ISOL-produced (Isotope Separation On-Line) beams [2]. The electron beam typically transports a current of 200 mA within a radius of 250 μm, corresponding to 100 A/cm^2. During normal operation the electron beam energy in the trapping region of the EBIS is approximately 4 keV. The emittance of the EBIS is strongly governed by the thermal energy of the ions in the radial potential well, while the contribution from the magnetic field strength of the EBIS solenoid is relatively small. The normalized RMS emittance contribution from the radial ion temperature ε_T [3] and magnetic field ε_{mag} [4] can be estimated by the following equations:

$$\varepsilon_T = \frac{r_{e^-}}{2}\sqrt{\frac{kT_{ion}}{m_{ion}c^2}} = 0.013\ \mu\text{m}$$

$$\varepsilon_{mag} = \frac{qB}{8m_{ion}c}r_{e^-}^2 = 0.0013\ \mu\text{m}$$

with q, m_{ion} and kT_{ion} being the ion's charge, mass and transverse temperature, r_{e^-}, the electron beam radius and B, the magnetic field strength in the EBIS trapping region. The values above are typical numbers for our setup, assuming, ions with mass number $A = 20$, charge state $Q = 5$, temperature $kT_{ion} = 200$ eV and a 2 T solenoidal field.

In order to velocity match the injection of the into the RFQ, the ion extraction potential is adjusted to $U_{ext} = 5 \cdot \frac{A}{Q}$ kV. After charge breeding in the EBIS, the ion beam is focused in two Einzel lenses (80 mm inner diameter) before being separated by A/Q in an achromatic Nier-type spectrometer made up of an electrostatic and a magnetic bender [5,6]. The emittance meter was installed at different positions (see Fig. 1), before mass separation of the beam (see also Fig. 9 for detailed view) and after the separator, before the last quadrupole quadruplet before the accelerating RFQ (see [5,6] for details on ion optics).

Knowledge of the beam emittance is of importance for beamline, separator and accelerator design, but also for the setup of the experimental stations. In the past there have been several attempts to measure the REXEBIS emittance with different methods. According to simulations, the non-normalized acceptance of the separator is 20 μm for a 5 keV/u beam [6]. Previous measurements yielded non-normalized emittances (95%) of 20 μm before mass separation [7] and 10–15 μm after the separator magnet [8] for a 5 keV/u beam ($\beta = 0.003$). After the normal conducting linac, a significantly higher normalized RMS emittance of 0.04–0.05 μm was measured with the slit-grid method [9]. Most of these measurements, however, were carried out with a highly space-charge compensated electron beam in order to increase the signal at the emittance meter, which may have inflated the emittance value compared to normal operation. In addition, the still poor signal-to-noise ratio might have altered the emittance value. This uncertainty has called for a more rigorous attempt to establish an emittance value

* Corresponding author.
E-mail address: fredrik.wenander@cern.ch (F. Wenander).

https://doi.org/10.1016/j.nima.2018.12.072
Received 31 May 2018; Received in revised form 20 December 2018; Accepted 20 December 2018
Available online 26 December 2018

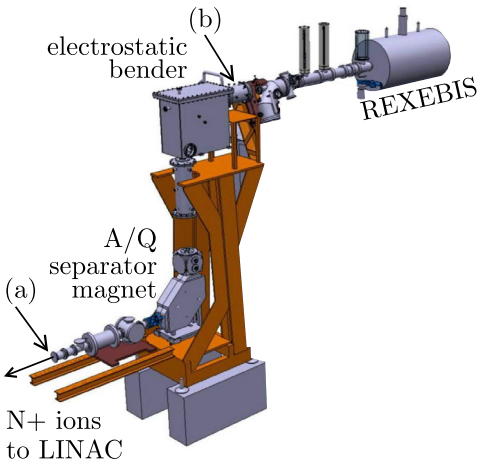

Fig. 1. REX-ISOLDE low-energy stage. Ions from the EBIS undergo electric and magnetic deflection in the Nier-type spectrometer. The measurement positions (a) after and (b) before mass separation are indicated.

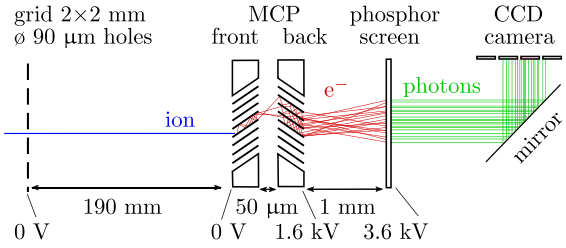

Fig. 2. Schematic drawing of the different detection stages and transverse signal spread in the pepperpot emittance meter (not to scale). Reference settings for the MCP and phosphor voltages are indicated.

for operational conditions. This article presents measurements of the emittance of the charge breeder before and after mass separation, while at the same time a measurement campaign takes place after the HIE-ISOLDE linac installation, in order to resolve inconsistencies.

2. Emittance meter setup

In this article we present measurements of the transverse emittance of beams from REXEBIS with a pepperpot emittance meter. In such a device, a mask in the form of a square grid of microscopic holes is used to split the beam into numerous small beamlets of which each samples a specific position in the transverse beam profile. The beamlets propagate through a drift space of length L before hitting a position sensitive detector and producing an array of (non-overlapping) spots. In the drift space, particles pick up transverse offsets with respect to the hole locations x_{h_i} due to their individual trajectory angles and hit the detector at slightly different positions x_d. Assuming infinitely small holes in the mask, the intensity profile of each spot directly yields information about the angular distribution of the particles within that specific beamlet, because each position on the detector can be associated with an angle $x' \approx (x_d - x_{h_0})/L$. Here h_0 indicates the hole corresponding to the observed beamlet. In this way, the detector image provides the angular distributions and beam intensity at the different sampling points x_{h_i}, which together approximate the xx' phase space distribution. The emittance can be calculated using the established rms-emittance definition $\epsilon = \sqrt{\sigma_x^2 \sigma_{x'}^2 - (\sigma_{xx'})^2}$. The 2nd moments σ are computed by integrating over all positions and angles resolved by the detector, using the intensity within each detector pixel as the statistical weights.

The pepperpot used in this article is similar to the device described in [10]. The pepperpot mask that divides the ion beam into multiple beamlets has holes at 2 mm pitch. It was manufactured by etching 90 µm diameter holes into a 100 µm thick copper foil which is sandwiched between two copper support plates with 0.5 mm diameter holes. The holes are slightly tapered with the smallest diameter on the back side of the plate. While detection of the beamlets with a scintillating screen is suitable for high beam intensities as in [11], an MCP is needed to detect weaker particle currents, where scintillators fail due to the low detection efficiency. A Chevron-type MCP and P46 phosphor screen (APD 2 PS 40/12/10/8 I 60:1 EDR P46) convert the ion signal into an optical signal. The latter is guided via a 45° silver-plated mirror towards a CCD camera (IMI Rhein Series IMB-147FT) outside the vacuum chamber, which is equipped with a zoom lens (MLH-10X). The MCP has channels with a diameter of 10 µm at 12 µm spacing. In contrast to the original design, described in [10], the distance between the pepperpot mask and the MCP had to be extended to allow for maximum size of the beamlets while maintaining proper separation of the spots. The mask-to-MCP distance can be adjusted in a range from 40 to 190 mm. For the presented data the maximum distance was used. In order to reduce stray light influence, the emittance meter was fitted with a telescopic light shield between mirror and camera window on the vacuum side. An anodized aluminum enclosure was added on the air side between window and camera.

Fig. 2 shows a schematic of the emittance meter detection chain with reference settings for the detector voltages. The pepperpot mask and MCP front are at ground potential while the MCP back as well as the phosphor screen are at positive, independently variable potentials. The pepperpot mask is electrically isolated to allow for current read-out.

When running the MCP with the reference voltages indicated in Fig. 2, the pepperpot emittance meter is optimized for measuring particle intensities of 10^5–10^6 particles per pulse. At higher particle intensities, the MCP gain has to be decreased. Alternatively, the beam intensity at the pepperpot can be reduced without changing the emittance from the source, by sampling the beam with fast electrostatic deflectors such that only a fraction of the beam reaches the emittance meter. As the deflector's switching time of 50 ns is small compared to the shortest sampling length (1 µs), the pulse length is reduced without having an effect on the emittance through beam steering.

For the analysis of the emittance pictures we use a modified version of the LabVIEW program used in [11,12], which has been updated to include further image filtering features. The calculation of the emittance from a pepperpot picture has been outlined above and detailed mathematical descriptions of the phase space reconstruction have been published [13]. Here, we lay out the key steps taken by the program used for our measurements to extract the phase space density from the camera image.

The first step is the beamlet identification procedure. An unprocessed bitmap picture is loaded (Fig. 3, top) and a peak finding algorithm operates on the horizontally and vertically integrated intensity signals, to identify the rows and columns of beamlets in the image (Fig. 3, bottom). The positions of the identified peaks are used to define a Region Of Interest (ROI) in the image and a set of horizontal and vertical lines, which split this ROI into rows and columns, effectively isolating the individual beamlets within rectangular tiles. This and subsequent steps taken by the program, rely on an accurate alignment of the axes of the square grid of holes in the mask with the axes of the camera sensor. The user has to assure that the automated peak detection and tiling is performed correctly and can support the algorithm by applying the median filter for removal of pixel artifacts, eliminate the average background noise and tune the peak detection thresholds (not to be confused with the threshold filter). The different filters and their effect on the computed emittance value are discussed in Section 3.4. To reconstruct the horizontal phase space, the pixel values within the ROI are integrated along the vertical axis (and vice versa for the vertical phase space). This step reduces the dimensionality of the data and preserves the required information because pixels in the same column correspond to the same horizontal position and angle. In order to

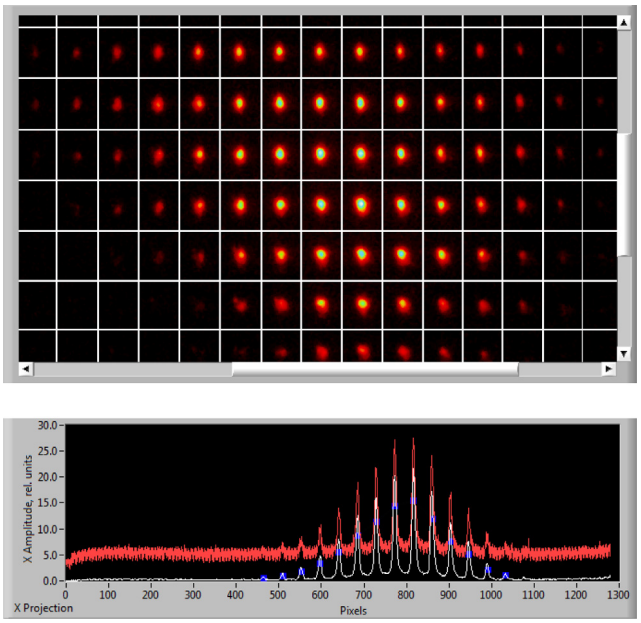

Fig. 3. Part of a loaded beamlet picture (top). The region of interest around each beamlet is isolated with horizontal and vertical lines. Projection of the beamlets along the vertical axis (bottom). The red trace shows the integrated signal without filters applied in the bitmap picture, the white trace shows the integrated signals with the median and offset filter applied. The blue crosses indicate peaks identified by the program. (For interpretation of the references to color in this figure legend, the reader is referred to the web version of this article.)

translate the image coordinates to real distances and compute the angles associated with each pixel, the user has to provide the mm/pix scaling factor alongside with the hole-to-screen distance and the hole-to-hole distance. The program chooses the intensity-weighted mean position of the beamlets as the coordinate zero point and as the position of the central hole. Each identified column of beamlets is then assigned the corresponding hole position x_{h_i} and the angles x' associated with each pixel can be computed. The measured intensities at these positions and angles approximate the phase space density profile. The choice of detector and hole coordinates can introduce a global positional and angular offset, but does not affect the second moments relevant for the emittance computation.

3. Methods

The signal of the initial ion beamlet impinging on the MCP is transformed and amplified several times. First it is converted into an electron signal in the MCP, then in the phosphor screen into a light signal which is finally registered with a CCD camera and saved as a picture. In order to obtain absolute measurements it is crucial to ensure linearity in every single step, such that the intensity distribution of the ion beamlet is transformed linearly into a pixel intensity with no alteration of shape. Only then is the picture truly representative of the ion beam emittance at the measurement position. Through careful tailoring of all detector parameters to the incoming ion beam current we could obtain reproducible measurement conditions and an excellent signal-to-noise ratio.

3.1. Current limitations

In the following we discuss the limitation from detector dead time and saturation on incoming ion beam intensities. In doing so, one has to keep in mind that the beam at REX-ISOLDE is pulsed with a low duty cycle. Even though integrated particle intensities are relatively low, the instantaneous particle rates during the short pulse can be significant.

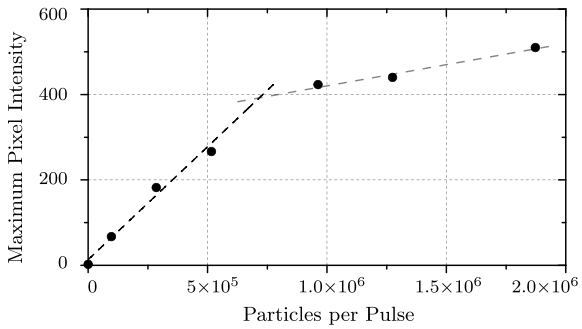

Fig. 4. Maximum pixel intensity after the mass separator with 1600 V gain on the MCP, for the particular ^{39}K beam described in the text. Linear fits to subsets of the data indicate the linear region and the saturation of the MCP above $7{\cdot}10^5$. Pixel intensities are lower than in Fig. 5 due to lower repetition rate.

A calculation similar as in [14] gives a recharging time of the MCP of approximately 1 ms for a resistance between the MCP front and back plate of 30 MΩ and a total number of 10^7 channels. As the typical ion extraction pulse width is only 0.3 ms, depleted channels cannot recover during the pulse. At too high particle intensities saturation of the MCP arises due to the dead time of the channels. However, the recharging time is small compared to typical repetition rates of 2–50 Hz, therefore the MCP will fully recover between successive EBIS pulses.

In order to calculate the maximum particle intensity before saturation of the MCP occurs, one has to take into account that the MCP is of the Chevron-type. We assume that the MCP gain is in a region where one signal-producing ion impinging on the MCP front will completely deplete one MCP channel of the first stage (single-particle counting). Between the two MCP stages there is a gap of 50 μm (see Fig. 2) where the electron avalanche spreads transversally. It triggers and completely depletes channels within an area of approximately 50 μm diameter on the second MCP, corresponding to 20 channels at a pore pitch of 12 μm [15]. Not every ion hitting the MCP will create an electron avalanche, which is expressed by the open area ratio of the MCP (0.63) and an ion conversion factor in the order of several 10% (here: 0.6) [15]. Taking these factors into account, the maximum acceptable particle density impinging on the MCP front is 1350 ions/mm^2 per pulse.

As an example for the occurrence of saturation we have examined a mass-separated ^{39}K beam (see Fig. 4). For this beam there were about 25 dominant beamlets, each of them with a FWHM of 300 μm, giving a total activated area of 1.8 mm^2. Assuming a uniform particle distribution over this area at the particle density calculated above and further dividing by the grid transparency of the mask ($1.6 \cdot 10^{-3}$), gives a total acceptable incoming ion current of $\sim 10^6$ particles per pulse before the pepperpot mask.

Fig. 4 shows the maximum pixel intensity for a varying particle intensity of this beam. The maximum pixel intensity is determined as the highest pixel value in the most dominant beamlet and taken as a measure of final signal intensity. Above 10^6 ions per pulse the MCP is indeed saturated, causing a non-linear amplification. On a case-by-case basis, the beamsize (i.e. the number of beamlets), as well as the spot size of a single beamlet, vary depending on the beam properties and tuning. Nevertheless, for all our mass-separated beams (^{22}Ne, ^{39}K, ^{40}Ar) the saturation rate was around 10^6 ions per pulse when running the MCP gain at 1600 V. At lower MCP voltages, saturation occurs at higher incoming particle intensities, as one ion only partially depletes an MCP channel.

Fig. 5 (bottom) shows several current scans similar to Fig. 4 for different MCP voltages (note that axes are inverted compared to Fig. 4). For the representation of the ion current in this data, we have normalized each current scan with the ion beam current at saturation which is indicated by the dashed line. The normalized data all fall on the same curve and the common saturation behavior at the same maximum

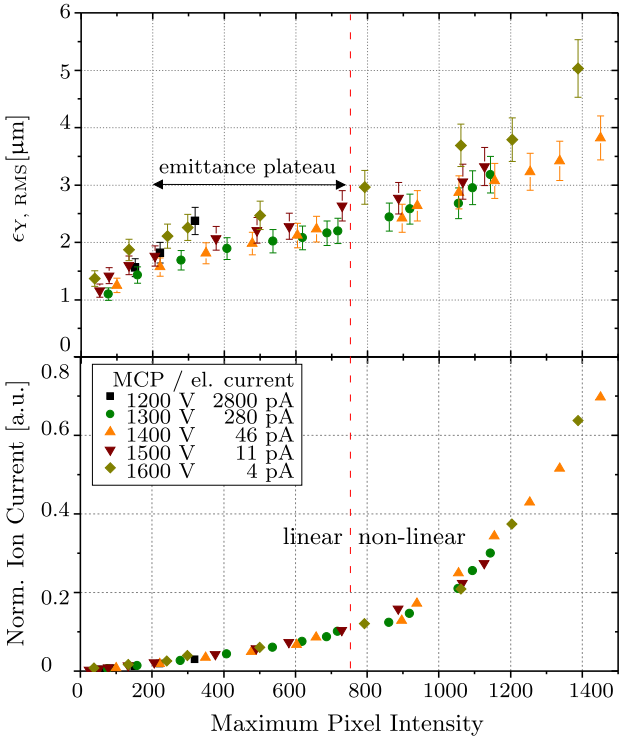

Fig. 5. Intermediate step in the emittance analysis. RMS emittance in vertical plane (top) and normalized ion beam current (bottom) as function of maximum pixel intensity. Here, the error bars represent the uncertainty coming from the noise filtering only. Ion currents have been normalized with the current right before saturation (values given in the legend). Within the plateau region the signal is translated and amplified linearly, resulting in a constant emittance value over all MCP voltages. Within this measurement series, all source settings remained constant; the particle intensity reaching the MCP was adjusted by sampling the beam with the electrostatic deflectors.

pixel intensity becomes apparent. The linearity always breaks down for the same maximum pixel intensity. This is because the MCP goes into saturation and cannot provide more electrons, thereby limiting the light output from the phosphor screen. Fig. 5 (top) shows the corresponding RMS emittances. Above saturation the non-linear signal amplification causes an overestimation of the emittance as the tails of the beamlet are amplified more than the beamlet center, resulting in an increased FWHM of the particle distribution. Below saturation the amplification is linear, resulting in a plateau of constant emittance. Most importantly the emittance value along the plateau does not depend on the MCP voltage. At too low particle intensities the analysis suffers from a low signal-to-noise ratio that causes an underestimation of the emittance value, as the noise filter cuts away a larger fraction of the signal. For all measurements presented in Section 4, we have chosen a working point in the plateau region, usually right before saturation, where the signal-to-noise ratio, which was approximately 100, was most favorable.

After the mass separator, beams of different mass, charge and energy were analyzed with the conclusion that the maximum pixel intensity is to the first order independent of these parameters, but determined only by the incoming particle density and detector settings. From a practical point of view, very high particle currents should be avoided as there is a risk of irreversibly damaging the phosphor screen.

3.2. Detector parameters

The detector voltages have to be adapted to the desired particle intensities (or vice versa), such that a linear amplification and translation of ion current into a pixel signal is ensured.

The MCP gain, or electron amplification, is determined by the voltage difference between the MCP front and back plates. For a certain choice of MCP gain, the dynamic range of the emittance meter, in terms of incoming particle intensity, is strongly limited by the saturation behavior of the MCP. Therefore, before each measurement series, we have measured the amplification for varying incoming particle currents as shown in Figs. 4 and 5 (bottom) and thereafter chosen a working point within the plateau region, see Fig. 5 (top), right before saturation. In order not to alter the beamlet shape it is essential that this amplification curve is linear with zero offset, otherwise the emittance will be overestimated.

The phosphor voltage determines the acceleration potential of the electrons exiting the MCP towards the phosphor screen. We have found that this acceleration voltage is a linear parameter over a wide range, meaning that it does not affect the emittance value. However, it does influence the light output from the phosphor without introducing additional background and may therefore be used for enhancing the signal-to-noise ratio by maximizing the signal intensity.

Cameras usually offer the possibility of signal modification through a set of parameters like brightness, sharpness and gamma. These parameters are in general non-linear data manipulations. We found that the camera gain was indeed linear, but since the background is amplified by the same factor as the signal, it does not enhance the signal-to-noise ratio. We used the optional camera parameters only during the beam tuning, but disabled them for emittance measurements.

3.3. Transverse resolution

The transverse resolution of a beamlet on the picture is limited by the detection geometry. Firstly, it is limited by the distance between the MCP pores. Secondly, as already discussed above, the electron cloud from one channel spreads over approximately 20 channels on the second MCP stage due to the spacing between the MCP plates. Between the MCP and the phosphor there is a gap of 1 mm where the electron cloud broadens again, such that the resolution on the phosphor screen for one ion impinging on the MCP front is in the order of 100 µm [16]. Optimally, the size of the beamlets should be large compared to the transverse resolution, but at the same time the beamlets from adjacent mask holes must not overlap. Typical beamlet sizes are about 0.3–0.7 mm FWHM. To decrease the point spread function on the phosphor one could remove the spacer between the MCP stages, however, that will reduce the total gain and is therefore only possible if the intensity loss can be compensated by an increased current. The spatial resolution in the picture depends on the resolution of the camera, its distance to the screen and the zoom, which results in our setup in roughly 40 µm.

Besides the uncertainties due to detector resolution, the finite hole size of the pepperpot mask causes a systematic overestimation of the emittance value. While hole sizes in the µm region are technically feasible, the transmission of the pepperpot mask might become too small when measuring low particle intensities. In the phase space reconstruction procedure it is assumed that all particles in a beamlet originate from the center of the corresponding hole in the mask. This introduces a positional error δ_x and a corresponding angular error $\delta_{x'} = -\delta_x/L$ for each trajectory, where L is the distance between mask and detector. For a thin mask with identically shaped small holes, it can be assumed that δ_x is independent of x and x'. In this case the measured second moments of the phase space distribution that define the emittance are

$$\sigma_x^2 = \sigma_{x_0}^2 + \sigma_{\delta_x}^2$$

$$\sigma_{x'}^2 = \sigma_{x_0'}^2 + \sigma_{\delta_{x'}}^2 = \sigma_{x_0'}^2 + \sigma_{\delta_x}^2/L^2$$

$$\sigma_{xx'} = \sigma_{x_0x_0'} + \sigma_{\delta_x\delta_{x'}} = \sigma_{x_0x_0'} + \sigma_{\delta_x}^2/L,$$

where the 0 index denotes the moments of the error-free distribution. Inserting these identities into the definition of the emittance, yields a

correction formula that relates the true emittance to the measured beam parameters $[\sigma_x^2, \sigma_{x'}^2, \sigma_{xx'}] = \varepsilon \cdot [\beta, \gamma, -\alpha]$.

$$\varepsilon_0 = \sqrt{\sigma_{x_0}^2 \sigma_{x_0'}^2 - (\sigma_{x_0 x_0'})^2} = \sqrt{(\sigma_x^2 - \sigma_{\delta_x}^2)(\sigma_{x'}^2 - \sigma_{\delta_x}^2/L^2) - (\sigma_{xx'} - \sigma_{\delta_x}^2/L)^2}$$

$$\varepsilon_0 = \sqrt{\varepsilon^2 - \frac{\varepsilon\sigma_{\delta_x}^2}{L}\left(\frac{\beta}{L} + L\gamma - 2\alpha\right)} \approx \varepsilon - \frac{\sigma_{\delta_x}^2}{2L}\left(\frac{\beta}{L} + L\gamma - 2\alpha\right)$$

A similar and more detailed derivation of this correction for the case of a slit scanner can be found in [17]. In order to estimate $\sigma_{\delta_x}^2$ we assume that a particle has a uniform probability to pass the hole at any position (δ_x, δ_y) within the circular aperture. During the phase space reconstruction one of the transverse dimensions of the hole is eliminated by integration. Due to this, the offset in the remaining dimension δ_x follows a Wigner semicircle distribution. For such a distribution the variance $\sigma_{\delta_x}^2 = R^2/4$, where R is the hole radius. The correction has been applied to all measurements presented in this paper and is smaller than 2% in all cases.

In principle the finite thickness of the mask can cause an occlusion effect. As a result of large-angle particles being blocked by the walls of the holes, the emittance would appear smaller. However, in our case this effect is not of concern, since our beams are fairly parallel as is also reflected in the long distance of 19 cm between the mask and the MCP. In addition, the tapered hole shape mitigates the effect.

3.4. Noise filtering

Fig. 6 illustrates the behavior of signal and background for varying camera shutter times. Here, the EBIS is operated at 10 Hz and $5 \cdot 10^5$ particles per pulse, detector voltages are adjusted such that the measurement is within the emittance plateau, below saturation. As shown in Fig. 6 (bottom), the background does not change significantly for shutter times varying from 0.5 to 4 s. The calculated emittance remains approximately constant above 1 s shutter time. Below 1 s, the emittance is underestimated as the peaks disappear in the background. Hence, a long integration time should be chosen for a favorable signal-to-noise ratio. In a typical measurement below saturation of the MCP, using a shutter time of 4 s, the most intense peaks have pixel intensities in the order of some 100, depending on the repetition rate. We conclude that the bit depth is sufficient not to contribute significantly to the total error. The background is scattered around 5 with a standard variation of σ_B=1.2–1.6. The background level remains the same when the valve to the ion source is closed such that neither ions nor light from the cathode can reach the MCP. Background from the cathode light becomes relevant only outside the typical operating regime, at MCP voltages above 1900 V.

Before evaluating the emittance picture we apply a series of noise filters:

- *Median filter* substitutes every pixel with the median of the value of the pixel and its 8 surrounding pixels.
- *Offset filter* subtracts the same value in every pixel.
- *Threshold filter* sets all pixels below a certain threshold to zero, while pixels above the threshold maintain their values.

The median filter is applied to eliminate single faulty pixels, while the offset filter is used to subtract the mean background value, determined far outside the beam spot. The threshold filter is set such that the noise is sufficiently suppressed between the beamlets for proper distinction of the latter. Fig. 7 (top) demonstrates how the result of an emittance calculation changes continuously with the setting of the threshold filter. At too low threshold the noise contributes to the emittance value, causing an overestimation. When increasing the threshold filter setting, the apparent emittance first drops drastically and then decreases further with a constant slope, as the peak tails are gradually cut away. To compensate for this effect, the preliminary emittance value is determined by linear regression to zero threshold of the points after the fall-off where

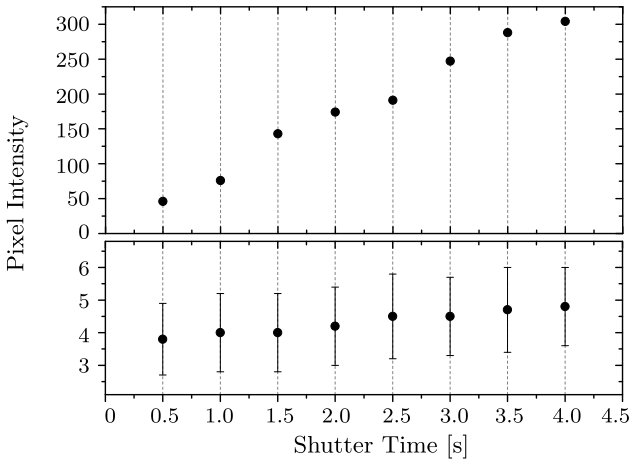

Fig. 6. Maximum pixel intensity (top) and background (bottom) as function of shutter time. The background is the mean pixel value in the picture area outside the beam spot. Error bars indicate the $\pm 1\sigma$ variation.

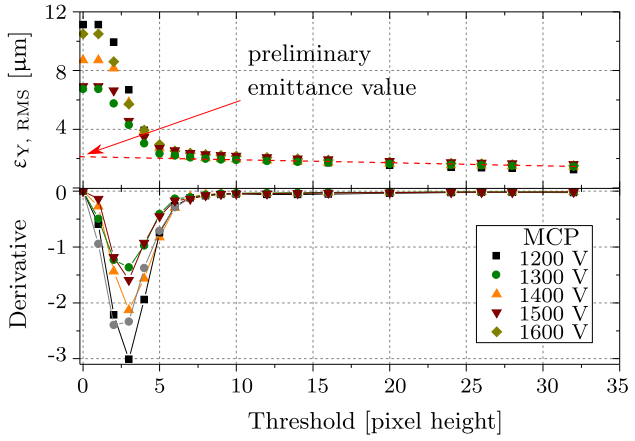

Fig. 7. Intermediate step in emittance analysis. Emittance (top) and its derivative (bottom) for different settings of the threshold filter. For too low filter settings the emittance is overestimated as the background is not sufficiently suppressed. At high threshold filter settings, the emittance value slowly decreases as the tails are gradually cut away. The preliminary emittance value is the intercept at zero threshold of the linear fit to the points after the fall-off (dashed line).

the slope is constant as indicated in Fig. 7. The finite-hole-correction needs to be applied to this preliminary value in order to arrive at the final emittance value.

3.5. Error discussion

Concerning the error of the final emittance value, we have earlier discussed non-linearities in the ion-to-pixel translation, limitations in the transverse detector resolution and filtering methods to suppress the noise. Apart from the previously pointed out sources of error we furthermore have uncertainties coming from the grid-to-MCP distance, imperfections in the hole circularity and the optical system (alignment of the mirror, lens and camera). For instance, a poorly adjusted camera focus introduces a significant error. In our setup the zoom-lens aperture remained fully open, resulting in a short focal depth. Therefore, the focus was adjusted for minimum size of the beamlets instead of on the frame of the MCP assembly. It is crucial to adjust the orientation of the camera to the rows of beamlet patterns, otherwise the beamlet distribution is broadened once the projection to the x/y-axes is performed. In a test measurement we set the mask-to-MCP distance to a minimum. The observed beamlets were circular with a width close to the hole diameter,

Table 1
RMS emittance measured at position (a) for different mass-separated beams for various extraction potentials U_{ext} and electron beam intensities. Numbers in brackets indicate the error bars on the last digit given.

Beam	e^- beam [mA]	U_{ext} [kV]	$\varepsilon_{X,RMS}$ [μm]	$\varepsilon_{Y,RMS}$ [μm]
$^{22}Ne^{6+}$	143	40	4.2(4)	4.4(4)
$^{39}K^{7+}$	143	20	4.4(4)	2.6(3)
$^{39}K^{10+}$	143	20	5.8(5)	3.8(4)
$^{39}K^{12+}$	143	20	7.3(7)	4.8(5)
$^{39}K^{11+}$	143	40	4.3(4)	3.8(4)
$^{39}K^{10+}$	235	40	7.4(7)	6.4(6)
$^{40}Ar^{13+}$	143	40	4.6(4)	3.7(3)
$^{40}Ar^{9+}$	143	40	4.5(4)	3.5(3)

leading to the conclusion that under our measurement conditions, the errors from optics and limitations in transverse resolution are negligible.

An important uncertainty comes from the detector settings and response. Within the emittance plateau of our test beam (see Fig. 5), where we expect a linear signal amplification, the 1σ-scattering of the emittance values within one measurement series is 2%. The scattering within all data points in the plateau across all MCP gain settings from 1200–1600 V is 6%. For this data, an error bar of 10% of the emittance value including these detector-related effects (non-linearities and choice of MCP voltage), as well as the uncertainty from the analysis (see Sections 3.3 and 3.4) is reasonable. In general, however, this depends strongly on the quality of the data and has to be adapted on a case-by-case basis. Significantly larger error bars have to be expected for a lower signal-to-noise ratio.

For the measurements shown in the next section, all detector and filtering parameters were optimized and the data analyzed and corrected for the finite hole size as explained above. The error bars shown are an estimation of the total error on the absolute value including all effects discussed in this section.

4. Results

4.1. Mass-separated beams

In measurement position (a) (Fig. 1) mass-separated beams of different elements and charge states were characterized. K^+ ions were injected from the local ion source into the EBIS and charge bred, while Ne and Ar ion beams were produced in the EBIS from neutral gas injection and residual gas, respectively. The separator beam optics were set up to maximize transmission of the selected A/Q through the mass slit. Table 1 gives the measured RMS emittance. All values are non-normalized and can be directly compared to values of non-separated beams measured in position (b), where a normalization is not possible due to the presence of multiple elements and charge states.

In these measurements no systematic difference between ions from injected 1^+-beams and from neutral gases could be observed. X-emittances are in general higher than Y-emittances owing to the selection at the mass slit in the vertical plane. Non-normalized RMS emittance values after the separator for beams of different elements and charge states are in the order of 3–7 μm and do not vary systematically between 20 and 40 kV extraction voltage. These observations lead to the conclusion that the beam is cut in the separator line at the 3 apertures used for differential pumping and mass separation, and that the beam from REXEBIS may exceed the acceptance of the separator. The non-normalized separator acceptance was simulated to be 20 μm [6] which is indeed in the order of the $4 \cdot \varepsilon_{RMS}$ measured non-normalized emittance. The beams with lower emittance values might as well be scraped. This can be explained by a non-ideal tuning resulting in a non-matched beam injection into the separator, which causes the limiting acceptance to appear to be smaller. Even though the source emittance could not be determined directly in this measurement position as the beam is scraped, the measured values are of interest. They describe the range of emittances that has to be matched with the RFQ, the first accelerating element after the separator, which has a transverse acceptance of 200 μm [6]. Furthermore, they support previous measurement carried out directly after the separator, and refutes the approximately 3 times higher values recorded in the linac.

4.2. Non-separated beams

As we experienced a cutting of the ion beam by beamline apertures when measuring in position (a), we moved the emittance meter closer to the EBIS, to point (b) in Fig. 1. In addition, the extraction potential was set to 35 kV – higher than the REXEBIS reference setting – in order to avoid cutting by apertures when performing tests with a highly neutralized electron beam where an increased emittance is expected.

The stable beam current originating from residual gases in the EBIS is in the range of 10^8 to 10^9 charges per pulse. Typical radioactive ion-beam intensities after the separator vary from a few ions to 10^8 ions per pulse at repetition rates ranging from 2 to 50 Hz. At these low ion beam intensities space charge neutralization of the electron beam does not play a role, as the total charge capacity of the REXEBIS electron beam is $1.9 \cdot 10^{10}$ elementary charges, for 150 mA electron beam, an electron energy of 4500 eV and a trapping length of 0.8 m. Neutralization is defined as the ratio of total extracted charges per pulse to electron space charge capacity. The total extracted current is measured after the electrostatic bender, where the extracted beam might have suffered from scraping. Therefore, the neutralization may be underestimated with as much as 20%. The ion beam intensities required to significantly neutralize the electron beam exceed typical intensities at REX-ISOLDE. For measurements with high ion beam intensities, the EBIS was filled with Xe gas via a precision leak valve to keep the particle number at a level that is not harmful for the detector. When using a heavy gas one can obtain a high level of space charge neutralization while keeping the particle intensities relatively low as the average charge state can be high (25^+ in this case with Xe). In addition, the deflectors were used, as described above, to sample the beam and control the number of particles reaching the MCP. In our measurements with Xe, neutralization levels up to 67% were achieved.

First, the emittance of the unseparated, Xe beam in point (b) was determined for a low level of neutralization, with no trace of cutting at apertures. At 12% neutralization an emittance of $\varepsilon_{X,RMS}$=4.1(5) μm and $\varepsilon_{Y,RMS}$=3.6(5) μm was measured. Assuming the major fraction of the beam consisted of Xe, with an average charge state of 25^+, the normalized emittance is 0.015(2) and 0.014(2) in the respective planes. This is in good agreement with the theoretical prediction given in the Introduction. The values in the horizontal and vertical plane do not differ significantly before separation, which is in accordance with our expectations, since the system is symmetric up to this point. As shown in Table 1, smaller and larger emittances have been measured after the separator compared to the emittance in point (b). Smaller emittance values stem from scraping at beamline apertures in the separator. Larger emittance values can partly be explained by aberrations in the beamline, however, the main effect most probably comes from the different beam composition in the two measurement cases. During the measurement in point (b), Xe outnumbered ions from residual gases. As Xe has relatively high charge states, the ions will in the ionization process be positioned on smaller radii inside the electron beam and thereby have smaller transverse emittance compared to residual gases.

Later, the neutralization was increased up to 67% by increasing the Xe injection rate. When running the EBIS with high electron beam neutralization, the trapping potential is more shallow and consequently the ions' radii are larger. Therefore an increased transverse emittance is expected. When measuring the beam emittance with high electron beam neutralization, strong aberrations were observed that manifest themselves as halos around the beamlets on the picture (see Fig. 8) and become more pronounced with higher degree of neutralization.

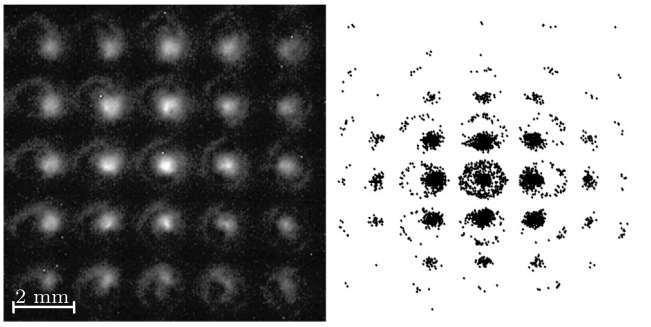

Fig. 8. Left: Emittance picture (zoom) of a Xe beam at 67% space charge neutralization. Right: SIMION simulation of a beam passing through an Einzel lens (filling factor 60%) and a pepperpot mask.

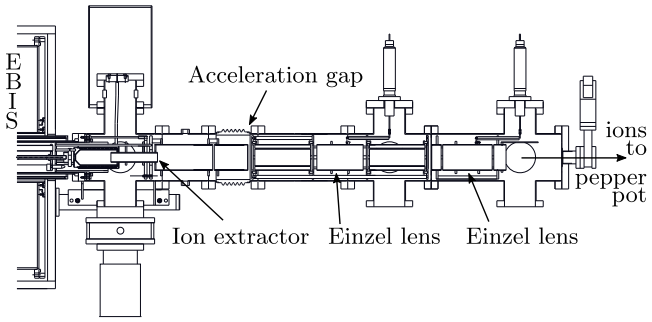

Fig. 9. Drawing of the REXEBIS extraction line. Elements with focussing properties are indicated. The second Einzel lens is the last active element before the pepperpot, which is located further downstream with some more drift space in-between.

A simulation revealed the cause of the halo-like pattern around the beamlets. The simulated test system consisted of a mono-energetic ion source, an Einzel lens, a pepperpot mask and an observation plane. This test system is simplified and not to scale compared to the real extraction system, shown in Fig. 9. In the simulation, the beam size was varied by changing the starting conditions of the ions. For filling factors of the Einzel lens – i.e. the ratio of beam to Einzel lens diameter – above 50%, spherical aberrations appeared. These spherical aberrations of the large-diameter beam in the Einzel lens in combination with the sampling of the beam at the pepperpot mask lead to a characteristic pattern of halos around the beamlets in the observation plane (see Fig. 8). The resemblance of the measured and simulated circular patterns indicate that the halos come indeed from spherical aberrations in our extraction system.

The emittance growth is reflected in the appearance of the halos. For pictures with strong halos the emittance can unfortunately not be quantified in a consistent way with our analysis method. A manual estimation, however, shows that the emittance grows at least by a factor 3 when increasing the compensation from initially 12% to 67% (Fig. 10).

5. Conclusions

We have characterized the beam from REXEBIS with a pepperpot emittance meter. Thereby we have carefully investigated the properties of the device and have established measurement and analysis procedures that lead to an excellent signal-to-noise ratio and stable, reproducible results. The emittance meter is being upgraded and will in the future feature a grid with smaller pepperpot holes (40 μm diameter) for better transverse resolution. The phosphor will be exchanged for a P43, which has a longer, but for our application sufficient, decay time of 1 ms (90%–10%) compared to the P46 (300 ns), but yields a higher light output which will improve the signal-to-noise ratio and detector sensitivity.

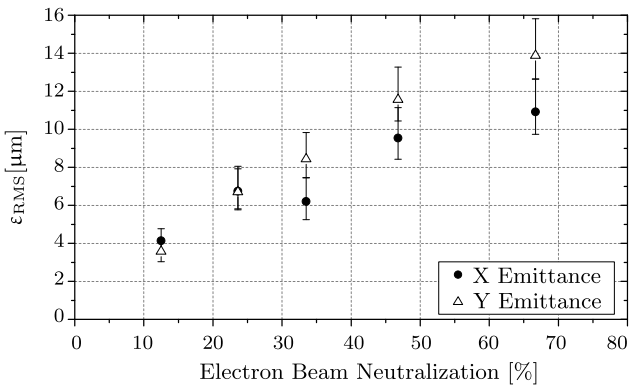

Fig. 10. RMS emittance of a Xe dominated cocktail beam measured in position (b) as function of electron beam neutralization. As the automatized analysis fails in the presence of the halos, the shown values are determined by a manual analysis of the pictures, therefore the error bars are larger.

RMS emittances of mass-separated Ne, K, and Ar beams after the REX separator range between 3 and 7 μm with a trend to higher values in the horizontal than in the vertical plane. The range of emittances agrees with previously determined values and therefore confirms previous measurements after mass selection. The measurements indicate that the beam is in some cases scraped by beamline apertures along the separator line. The RMS emittance of a non-separated beam with an extraction potential of 35 kV was determined to be 4 μm, which is in accordance with theoretical predictions. For space-charge neutralized electron beams in the EBIS, the ion beam emittance increases significantly. The data for the neutralized beams is more difficult to interpret as the large-diameter beams suffer from spherical aberrations in the extraction system. A simulation suggests that in the case of high compensation at least one of the Einzel lenses in our extraction system is filled to more than 50% in diameter.

The study has demonstrated that the beam emittance and transport can be easily compromised by cutting at apertures and by aberrations, especially at high neutralization. This serves as an important input for future beamline design. The newly designed extraction/injection line at the TwinEBIS test stand [18] will feature larger diameter beam line elements and gridded lenses instead of Einzel lenses to avoid the problems encountered at REX. With these measures taken, the full emittance beam can hopefully be transported even for high-intensity beams where a strong neutralization has to be assumed.

Acknowledgments

The authors would like to thank Argonne National Laboratory for the emittance analysis software.

This research project has been supported by the European Commission's Horizon 2020 Programme under contract number 642889 MEDICIS-PROMED. This project has received funding from the European Union's Horizon 2020 research and innovation programme under grant agreement No 654002. This work has been sponsored by the Wolfgang Gentner Programme of the German Federal Ministry of Education and Research (grant no. 05E15CHA).

References

[1] F. Wenander, B. Jonson, L. Liljeby, G.H. Nyman, REX-ISOLDE Collaboration Collaboration Collaboration, REXEBIS the Electron Beam Ion Source for the REX-ISOLDE Project, Tech. Rep. CERN-OPEN-2000-320, CERN, Geneva, 1998, URL http://cds.cern.ch/record/478399.

[2] R. Catherall, W. Andreazza, M. Breitenfeldt, A. Dorsival, G.J. Focker, T.P. Gharsa, G.T. J, J.L. Grenard, F. Locci, P. Martins, S. Marzari, J. Schipper, A. Shornikov, T. Stora, The ISOLDE facility, J. Phys. G: Nucl. Part. Phys. 44 (9) (2017) 094002, http://dx.doi.org/10.1088/1361-6471/aa7eba.

[3] P. Allison, J. Sherman, H. Smith, Comparison of Measured Emittance of an H- ion Beam with a Simple Theory, Los Alamos National Lab. NM (USA) LA-8808-MS, 1981, http://dx.doi.org/10.2172/6452992.

[4] V. Toivanen, T. Kalvas, H. Koivisto, J. Komppula, O. Tarvainen, Double einzel lens extraction for the JYFL 14 GHz ECR ion source designed with IBSimu, J. Instrum. 8 (05) (2013) P05003, http://dx.doi.org/10.1088/1748-0221/8/05/P05003.

[5] R. Rao, O. Kester, T. Sieber, D. Habs, K. Rudolph, Beam optics design of the REX-ISOLDE q/m-separator, Nucl. Instrum. Methods Phys. Res. A 427 (12) (1999) 170–176, http://dx.doi.org/10.1016/S0168-900298)01562-9.

[6] M. Fraser, D. Voulot, F. Wenander, Beam dynamics simulation of the REX-ISOLDE A/q-separator, CERN-ACC-NOTE- 2014-0017 HIE-ISOLDE-PROJECT-Note-0027. 2013. URL https://cds.cern.ch/record/1668145.

[7] F. Wenander, J. Cederkäll, B. Jonson, L. Liljeby, G. Nyman, K. Rensfelt, Ö. Skeppstedt, B. Wolf, REXEBIS, design and initial commissioning results, AIP Conf. Proc. 572 (1) (2001) 59–73, http://dx.doi.org/10.1063/1.1390100.

[8] S. Emhofer, F. Ames, J. Cederkäll, D. Habs, O. Kester, K. Rudolph, T. Sieber, Commissioning-results of the REX-ISOLDE linac, in: Proceedings of the Particle Accelerator Conference PAC2003, Vol. 5, 2003, pp. 2869–2871, http://dx.doi.org/10.1109/PAC.2003.1289749.

[9] D. Voulot, M. Fraser, D. Lanaia, T. Olsson, Transverse emittance measurements of the REX-ISOLDE beams in preparation for the HIE-ISOLDE commissioning, in: Proceedings of the Linear Accelerator Conference LINAC2014, Geneva, Switzerland, TUPP037, 2014, pp. 513–517, URL http://jacow.org/LINAC2014/papers/tupp037.pdf.

[10] A. Pikin, A. Kponou, J. Ritter, V. Zajic, Pepper Pot Emittance Meter, BNL Technote C-A/AP/#244. URL https://www.bnl.gov/isd/documents/80061.pdf.

[11] S. Kondrashev, A. Barcikowski, B. Mustapha, P. Ostroumov, N. Vinogradov, Development of a pepper pot emittance probe and its application for ECR ion beam studies, Nucl. Instrum. Methods Phys. Res. A 606 (3) (2009) 296–304, http://dx.doi.org/10.1016/j.nima.2009.04.050.

[12] S. Kondrashev, A. Barcikowski, A. Levand, P. Ostroumov, R. Pardo, G. Savard, R. Scott, T. Sun, R. Vondrasek, G. Zinkann, Emittance measurements for stable and radioactive ion beams, in: Proceedings of Linear Accelerator Conference LINAC2010, Tsukuba, Japan, TUP086, 2010, pp. 608–610, URL http://accelconf.web.cern.ch/AccelConf/LINAC2010/papers/tup086.pdf.

[13] H.R. Kremers, J.P.M. Beijers, S. Brandenburg, A pepper-pot emittance meter for low-energy heavy-ion beams, Rev. Sci. Instrum. 84 (2) (2013) 025117, http://dx.doi.org/10.1063/1.4793375, URL http://aip.scitation.org/doi/10.1063/1.4793375.

[14] J. Wiza, Microchannel plate detectors, Nucl. Instrum. Methods 162 (1) (1979) 587–601, http://dx.doi.org/10.1016/0029-554X(79)90734-1.

[15] Technical Information MCP Assembly, Hamamatsu Photonics K.K., Electron Tube Division, 314-5, Shimokanzo, Iwata City, Shizuoka Pref., 438-0193, Japan, 2006. URL http://www.triumf.ca/sites/default/files/Hamamatsu%20MCP%20guide.pdf.

[16] S.D. Pinto, R. Ortega, S. Ritzau, D. Pasquale, B. Laprade, S. Mrotek, S. Gardell, Z. Zhou, J. Plomp, L. Eijck, H. Bilheux, I. Dhiman, Neutron imaging and tomography with MCPS, J. Instrum. 12 (12) (2017) C12006, http://dx.doi.org/10.1088/1748-0221/12/12/C12006.

[17] R.L. Gluckstern, Notes on Beam Dynamics in Linear Accelerators, Tech. Rep. LA-8526-MS, Los Alamos Scientific Laboratory, Los Alamos, 1980, URL https://inis.iaea.org/search/search.aspx?orig_q=RN:12581986.

[18] M. Breitenfeldt, R. Mertzig, J. Pitters, A. Shornikov, F. Wenander, The TwinEBIS setup: Machine description, Nucl. Instrum. Methods Phys. Res. A 856 (2017) 139–146, http://dx.doi.org/10.1016/j.nima.2016.12.037.